

Supplementary Material

Accounting for uncertain fault geometry in earthquake source inversions – II: application to the Mw 6.2 Amatrice earthquake, Central Italy

Théa Ragon¹, Anthony Sladen¹ and Mark Simons²

¹ Université Côte d'Azur, CNRS, Observatoire de la Côte d'Azur, IRD, Géoazur, 250 rue Albert Einstein, Sophia Antipolis 06560 Valbonne, France.

² Seismological Laboratory, California Institute of Technology, 1200 E California Blvd., Pasadena, CA 91125-2100, USA.

You will find in the following pages:

page 2. Tables detailing the main characteristics of the InSAR images used in this study, as well as tables of residuals of the different inversions performed.

pages 3 to 16. Supplementary figures for the analysis of Bayesian inversion tests and results.

Satellite (orbit pass)	Track	Interferogram pair	Mean incidence angle
ALOS 2 (ascending)	A197	09/09/2015 - 08/24/2016	41.6°
ALOS 2 (descending)	D092	05/25/2016 - 08/31/2016	36.3°
Sentinel 1A (ascending)	TN117	08/15/2016 - 08/27/2016	24.8°
Sentinel 1A (descending)	TN095	08/14/2016 - 08/26/2016	17.5°

TABLE S1 – Interferometric pairs used in this study

	Fault geometry A no \mathbf{C}_p	Fault geometry B no \mathbf{C}_p	Fault geometry A \mathbf{C}_p	Fault geometry B \mathbf{C}_p
GPS	0.279	0.318	0.376	0.367
ALOS ascending	1.73	2.67	1.91	4.83
ALOS descending	2.62	3.48	3.33	5.08
Sentinel ascending	4.16	5.02	5.54	7.16
Sentinel descending	2.99	2.30	4.13	2.44

TABLE S2 – Residuals between observations and predictions (RMS in centimetre) for models inferred assuming fault geometries A and B, accounting or not for \mathbf{C}_p .

	no \mathbf{C}_p	$\mathbf{C}_p^{\text{fault}}$	$\mathbf{C}_p^{\text{fault}} + \mathbf{C}_p^{\text{earth}}$
Synthetic GPS	0.228	0.245	0.408
Synth. ALOS ascending	2.19	2.55	3.31
Synth. ALOS descending	1.77	2.48	2.84
Synth. Sentinel ascending	2.01	2.52	3.46
Synth. Sentinel descending	2.46	2.82	4.02

TABLE S3 – Residuals (RMS in centimetre) for the synthetic inversion with the first target model, assuming a wrong dip of 10° and an incorrect crustal structure, accounting or not for \mathbf{C}_p in fault geometry or/and crustal structure.

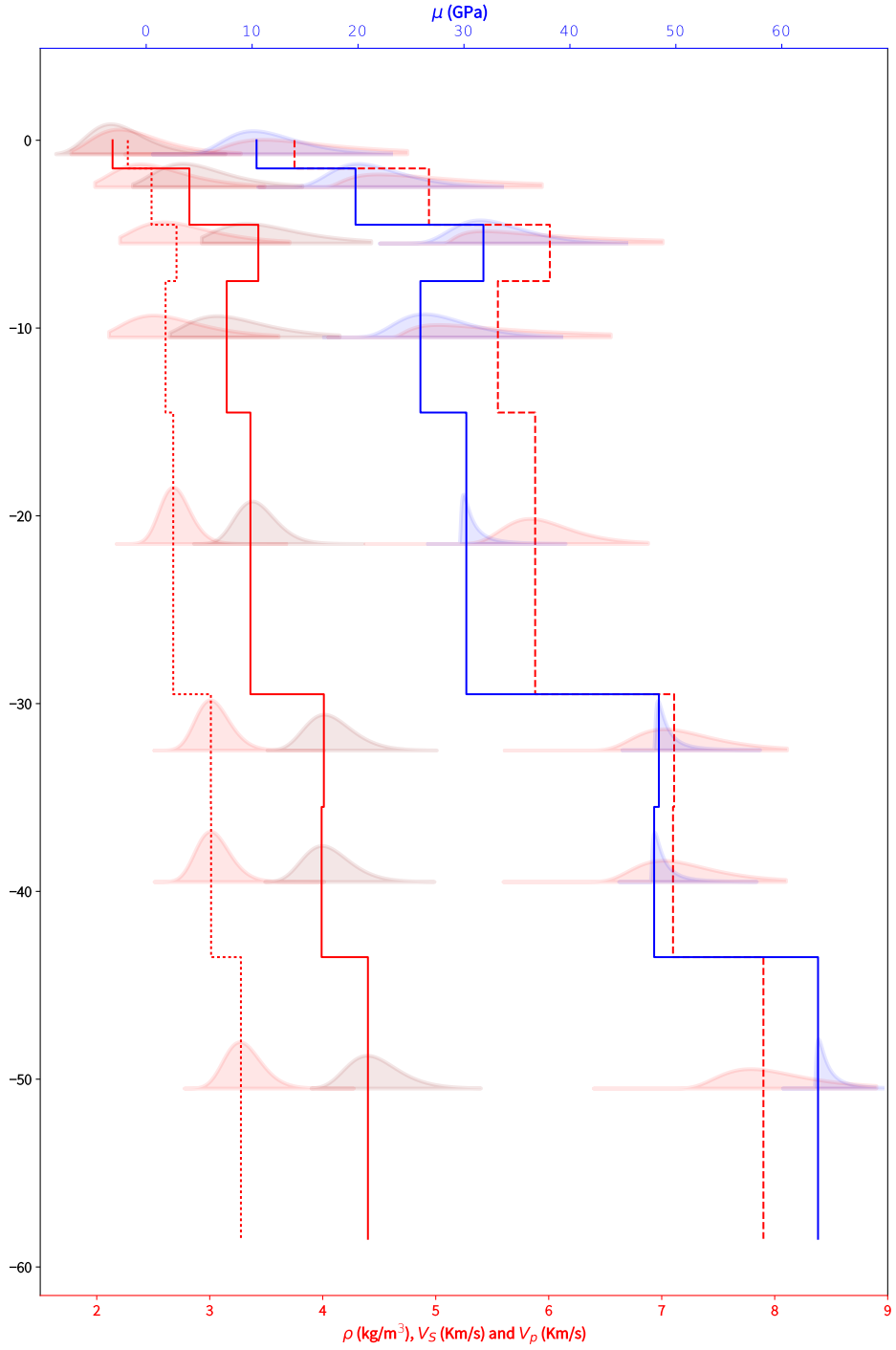


FIGURE S1 – Assumed elastic properties of the Earth and their associated uncertainties. V_s is illustrated with a red line, V_p with a dashed red line, ρ with a dotted red line and their values are detailed in the bottom axis. μ is illustrated by a blue line and legended in the top of the figure. The uncertainties associated with each parameter are also illustrated. The distribution of elastic parameters are log-normal, because the elastic parameters are Jeffrey's parameters (Tarantola et al. 2005, Duputel et al. 2014). λ is estimated from V_p , V_s , ρ and μ and thus its distribution derives from the distribution of these parameters.

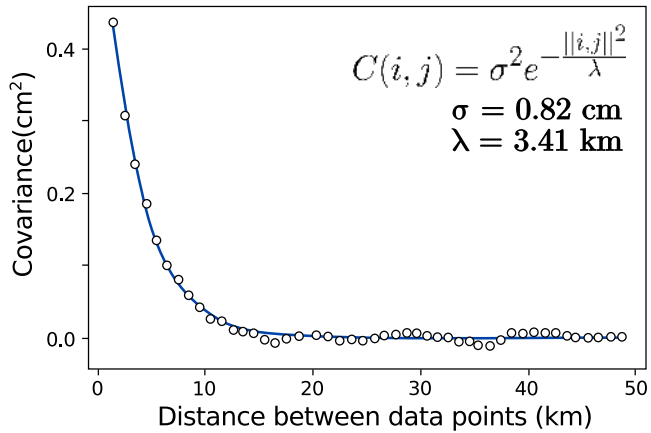


FIGURE S2 – Empirical covariance functions for the ALOS 2 descending interferogram. Radially symmetric empirical covariance functions and associated best fit exponential functions for the displacements derived from InSAR data. For each interferogram, we compute the empirical covariance as a function of the inter-pixel distance and then fit an exponential function (Jolivet et al. 2012). The exponential function is used to build the data covariance matrix.

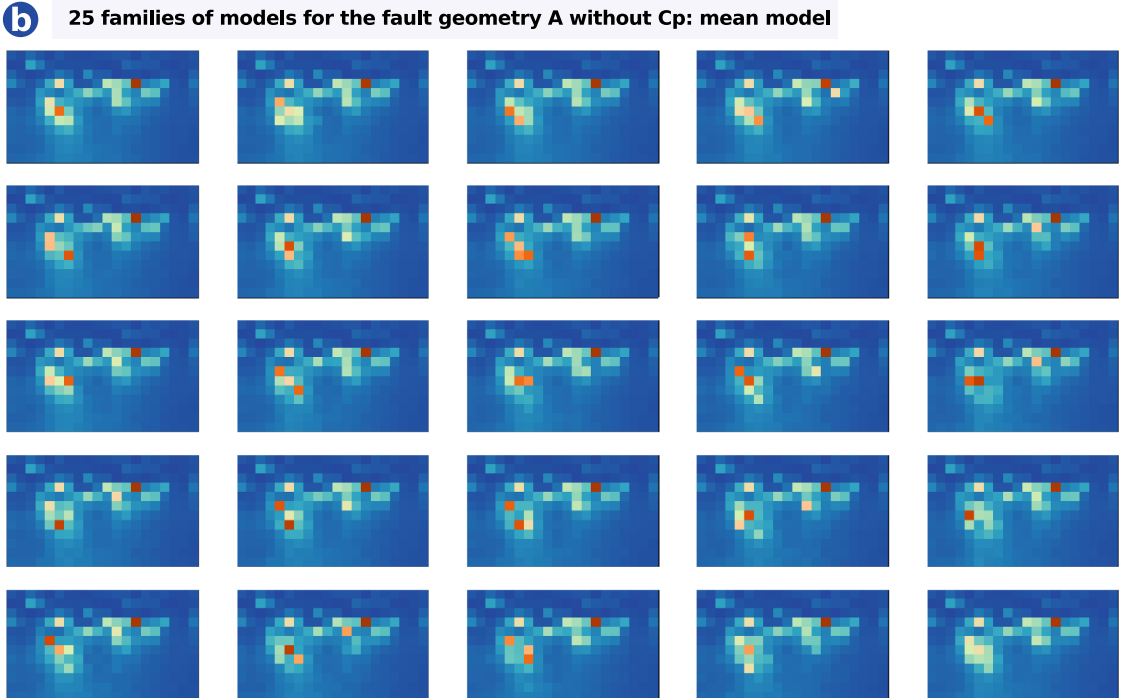
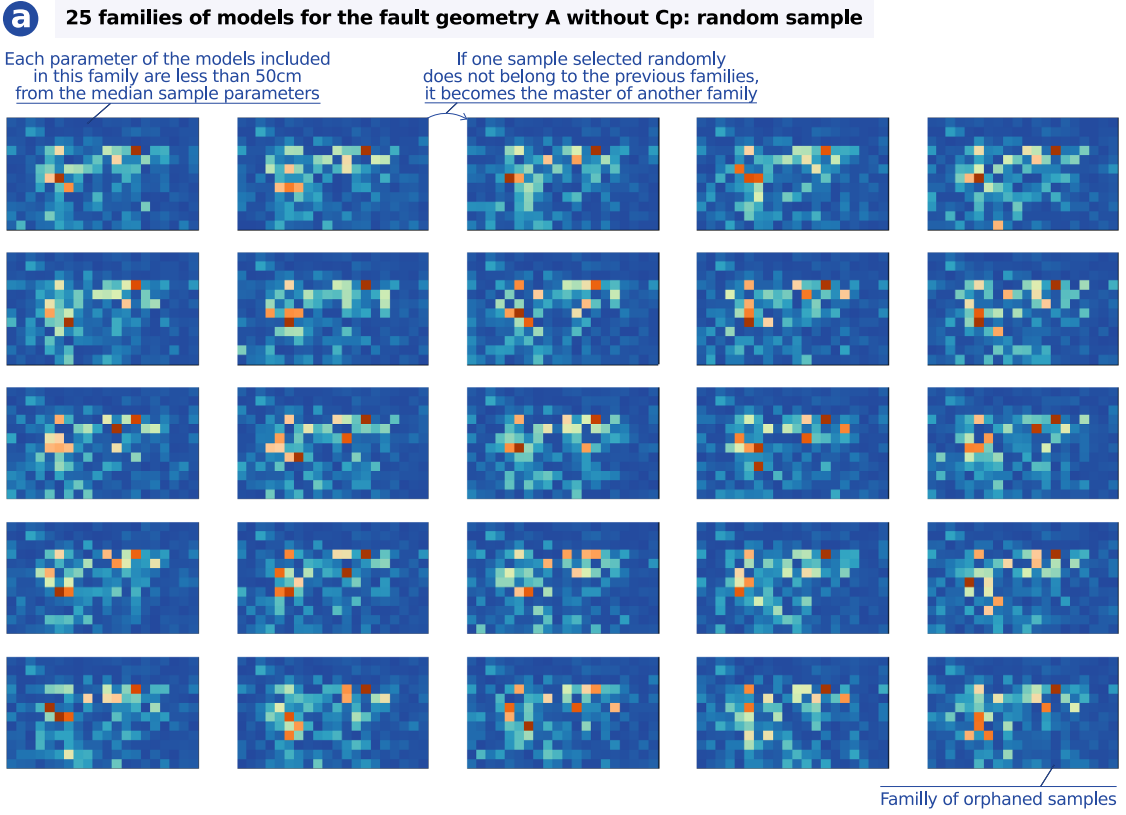


FIGURE S3 – The set of samples inferred from an inversion is divided into 25 subsets. The first family gathers samples whose parameters are of less than 50 cm offset from the median model parameters. In detail, a model is added to the first family if the selected model and the median model are parameter-wise equal within a relative tolerance of 20% added to an absolute tolerance of 50 cm for the co-seismic slip, and a relative tolerance of 10% added to an absolute tolerance of 25 cm for the post-seismic slip. Other families are built iteratively around a randomly selected model that has not fitted within antecedent families, except for the last family which regroups orphan samples. In (a), one model of each subset inferred without accounting for C_p and assuming fault geometry A is selected randomly. In (b), the median model of each of the 25 subsets is shown. In the main text, Figs 2c-d, 4a-h, 5a-b and 6c-d derive from the combination of random models –as in (a)– while Figs 10a-f are obtained from the combination of median models –as in (b).

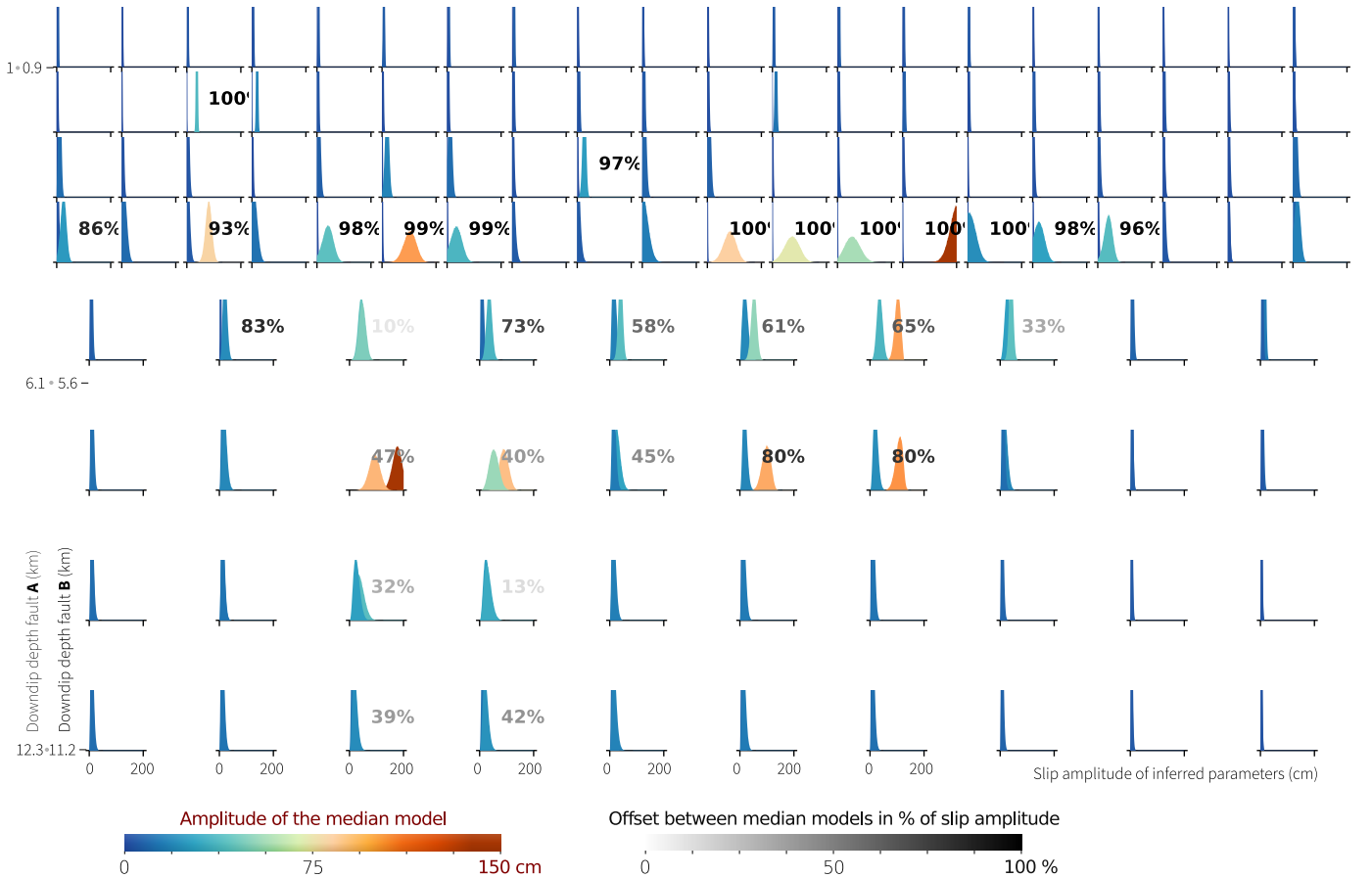


FIGURE S4 – Comparison between posterior marginal probability density functions of the dip-slip parameters inferred with fault geometry A and B. Parameters inferred assuming fault geometry A are in the foreground. In the last four rows, the PDFs show the repartition of parameters for patches covering 2 subfaults along strike and 2 subfaults along dip (i.e. patches two times bigger than for the first four rows). The offset between the median models is shown as percentage with a different color scale.

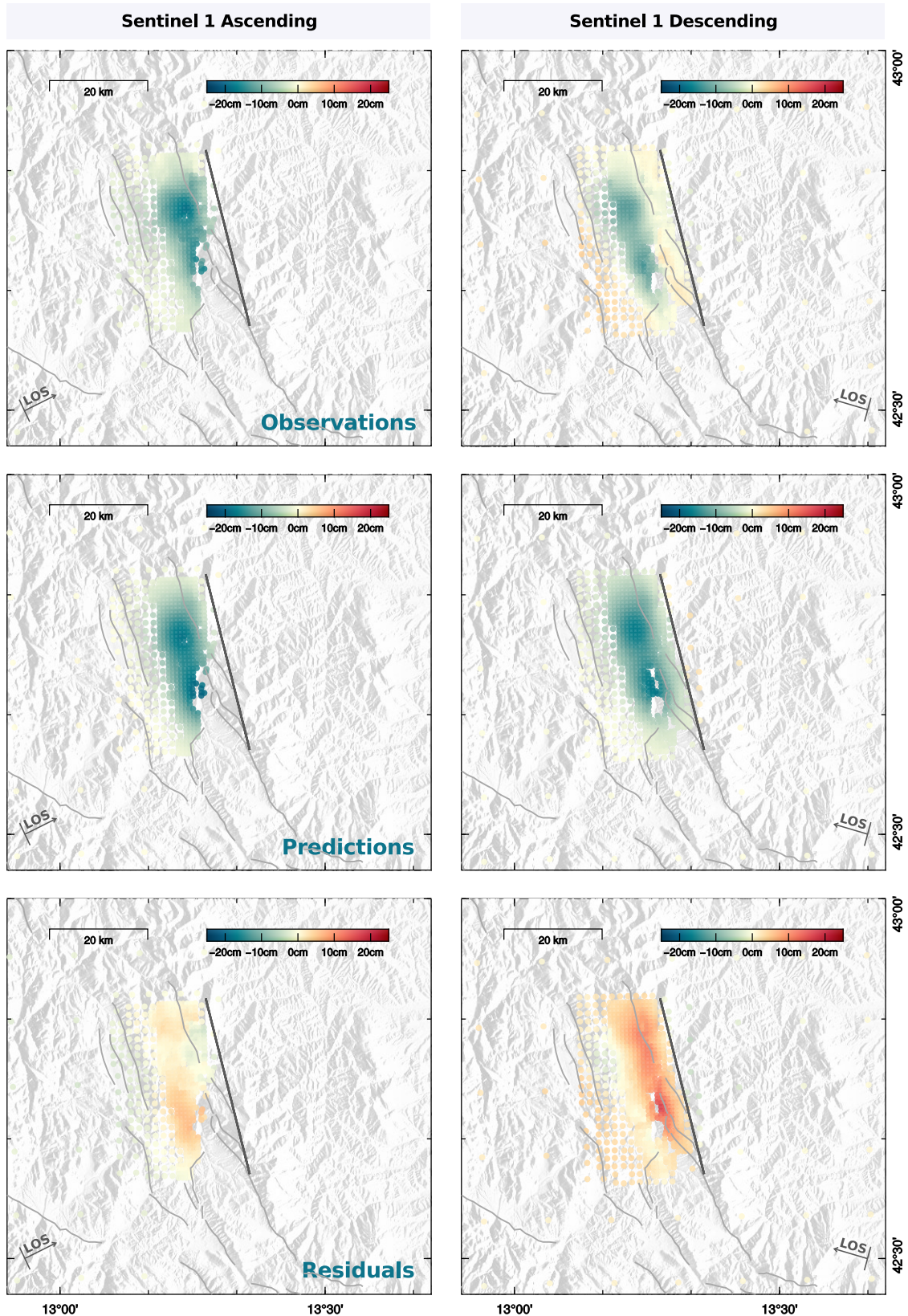


FIGURE S5 – Fit of the InSAR Sentinel dataset for an inversion made assuming fault geometry B and no C_p . Observations, predictions inferred from the average model and residuals are shown for Sentinel 1 ascending and descending interferograms, respectively to the left and to the right. The assumed fault trace is shown with a dark gray line. Seismogenic faults are shown in light gray.

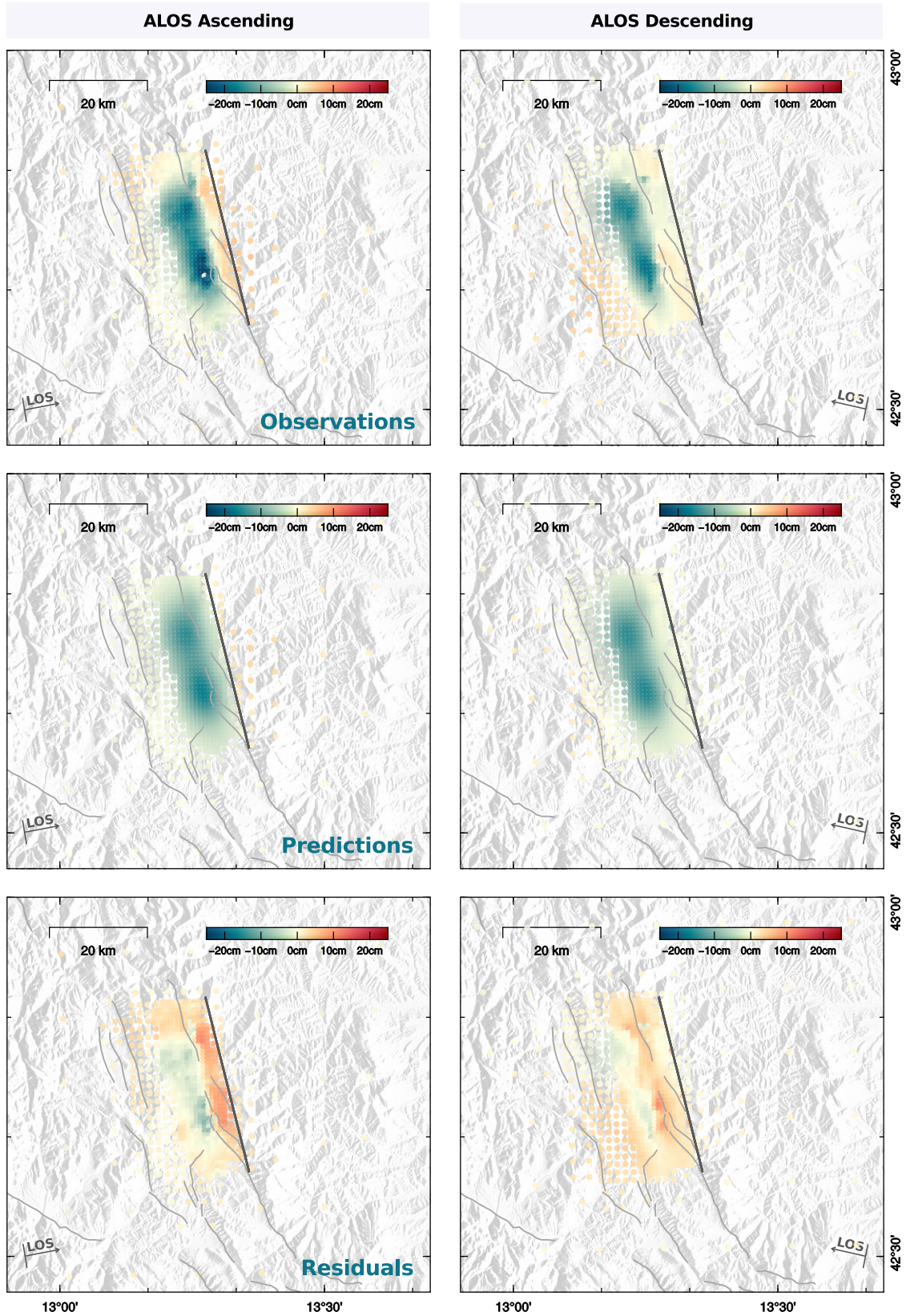


FIGURE S6 – Fit of the InSAR ALOS dataset for an inversion made assuming fault geometry B and no C_p . Observations, predictions inferred from the average model and residuals are shown for ALOS 2 ascending and descending interferograms, respectively to the left and to the right. The assumed fault trace is shown with a dark gray line. Seismogenic faults are shown in light gray.

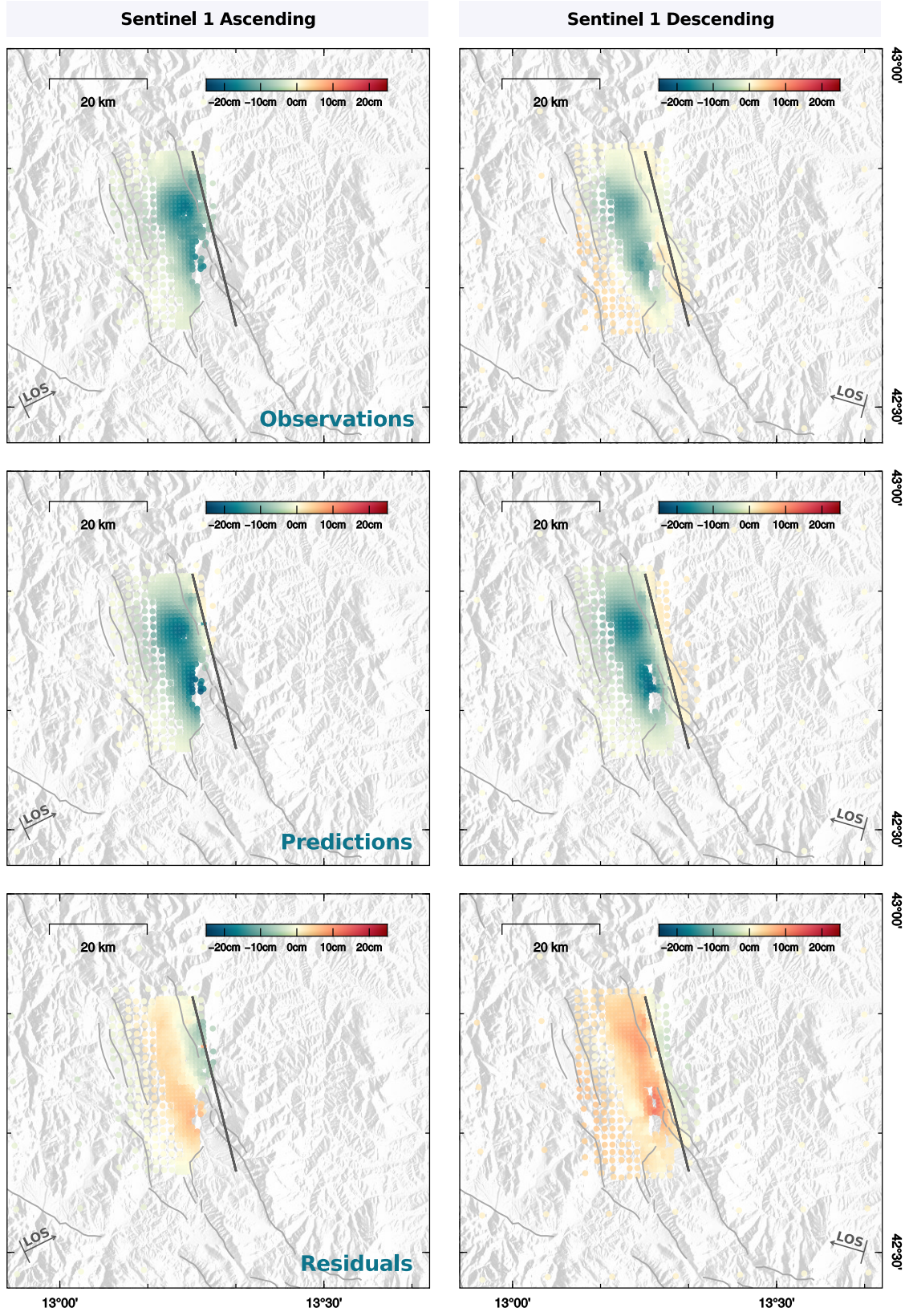


FIGURE S7 – Fit of the InSAR Sentinel dataset for an inversion made assuming fault geometry A and no C_p . Observations, predictions inferred from the average model and residuals are shown for Sentinel 1 ascending and descending interferograms, respectively to the left and to the right. The assumed fault trace is shown with a dark gray line. Seismogenic faults are shown in light gray.

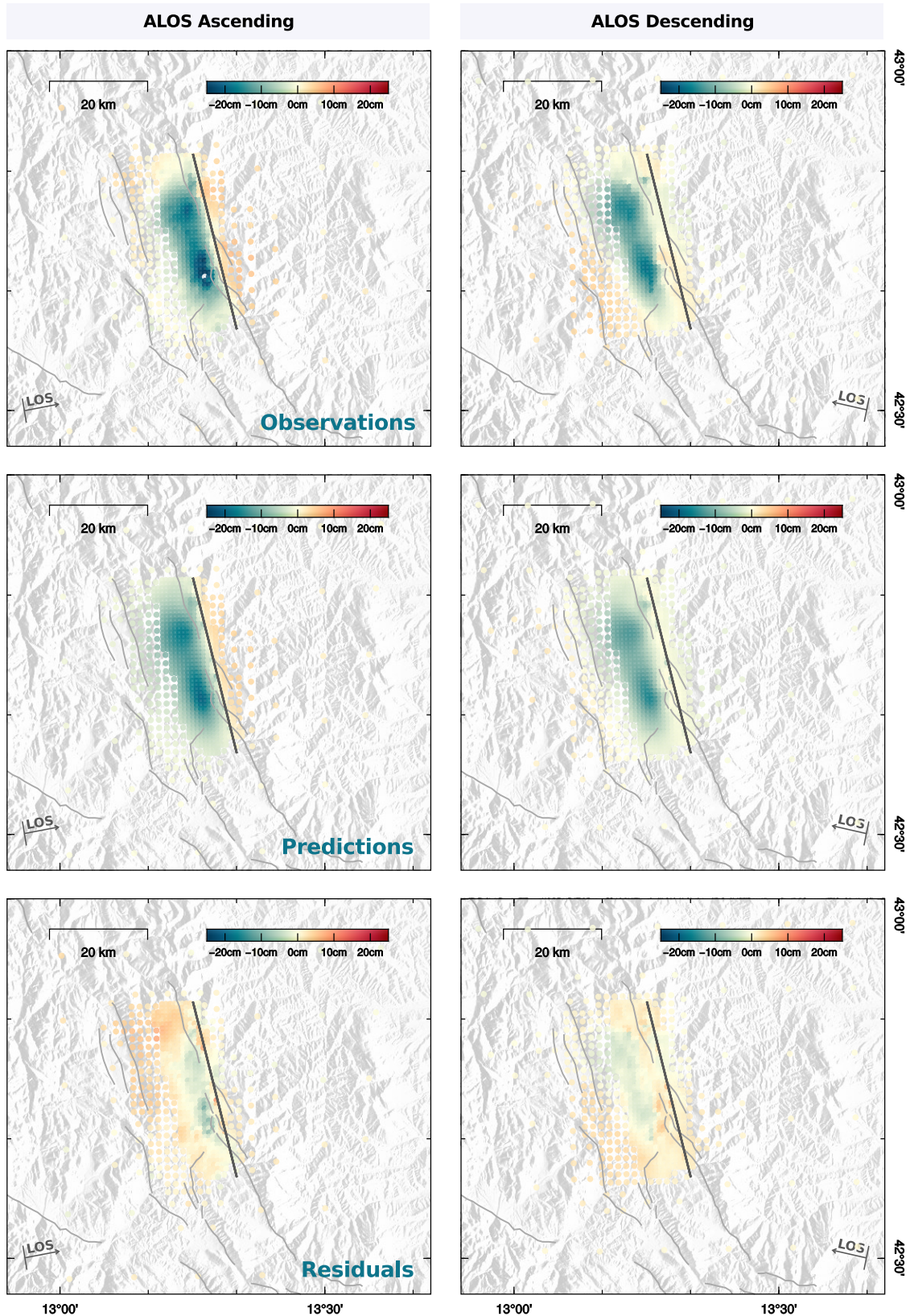


FIGURE S8 – Fit of the InSAR ALOS dataset for an inversion made assuming fault geometry A and no \mathbf{C}_p . Observations, predictions inferred from the average model and residuals are shown for ALOS 2 ascending and descending interferograms, respectively to the left and to the right. The assumed fault trace is shown with a dark gray line. Seismogenic faults are shown in light gray.

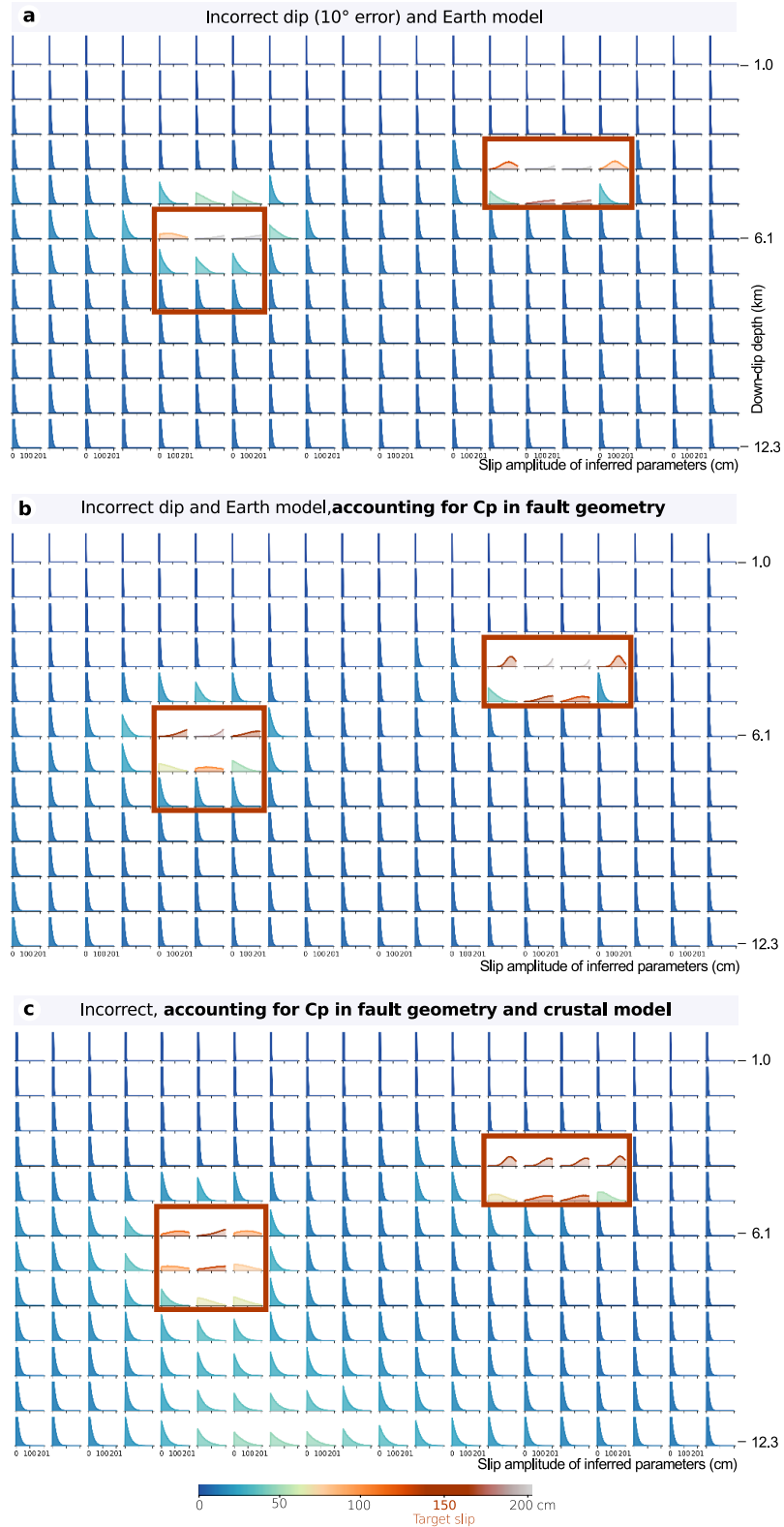


FIGURE S9 – Comparison of three finite-fault slip models inferred from the target model illustrated in Fig. 4(a), assuming an incorrect fault dip of 10° (with the position of fault A) and an incorrect elastic structure. In (a), we do not assume any uncertainties. In (b), we account for C_p^{fault} and in (c) for $C_p^{\text{fault+earth}}$. Each figure illustrate the posterior marginal probability density functions of the inferred models, and the target slip model is delineated with a red line.

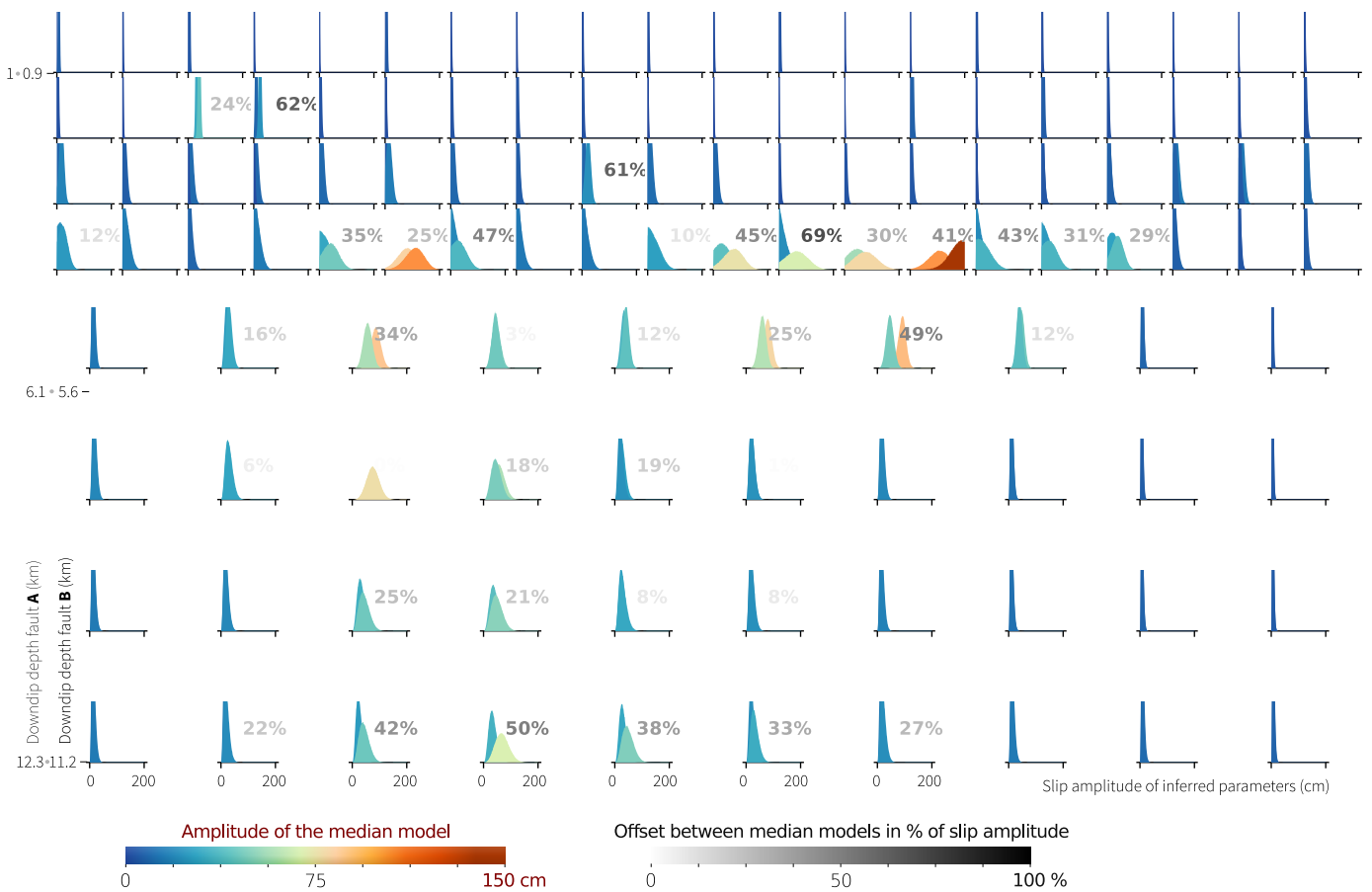


FIGURE S10 – Comparison between posterior marginal probability density functions of the dip-slip parameters inferred with fault geometry A and B, accounting for \mathbf{C}_p in fault geometry. Parameters inferred assuming fault geometry A are in the foreground. In the last four rows, the PDFs show the repartition of parameters for patches covering 2 subfaults along strike and 2 subfaults along dip (i.e. patches two times bigger than for the first four rows). The offset between the median models is shown as percentage with a different color scale.

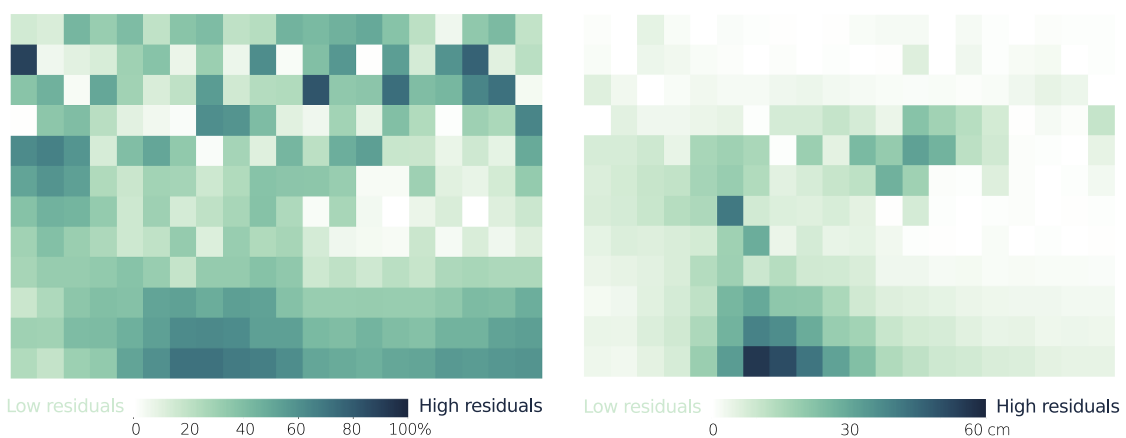


FIGURE S11 – Comparison of the residuals between inversion accounting or not for \mathbf{C}_p and with fault geometry A as reference. The residuals corresponding to dip-slip amplitudes of average models are presented in terms of percentage of slip (left) or as absolute values (right).

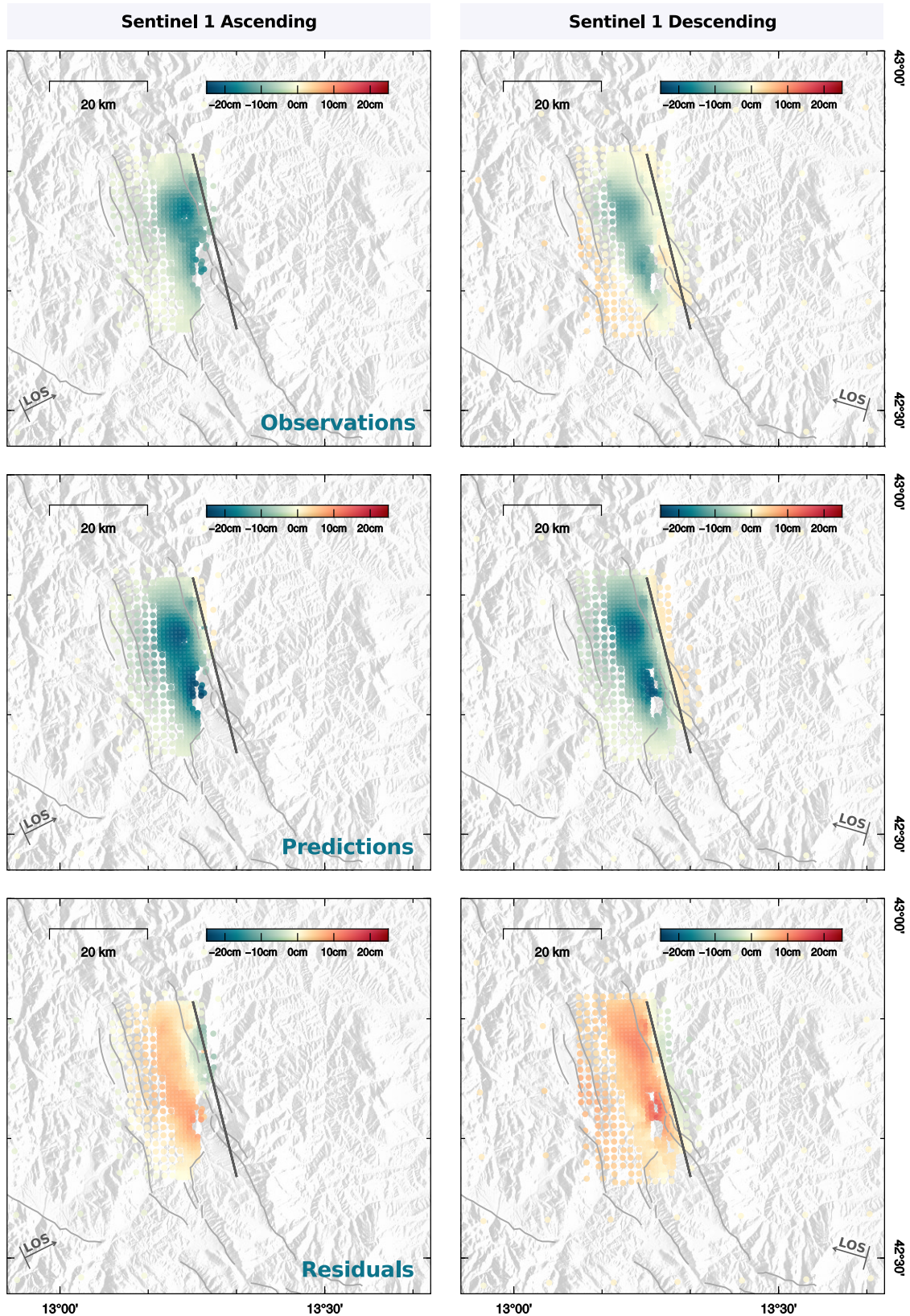


FIGURE S12 – Fit of the InSAR Sentinel dataset for an inversion made assuming fault geometry A and accounting for C_p . Observations, predictions inferred from the average model and residuals are shown for Sentinel 1 ascending and descending interferograms, respectively to the left and to the right. The assumed fault trace is shown with a dark gray line. Seismogenic faults are shown in light gray.

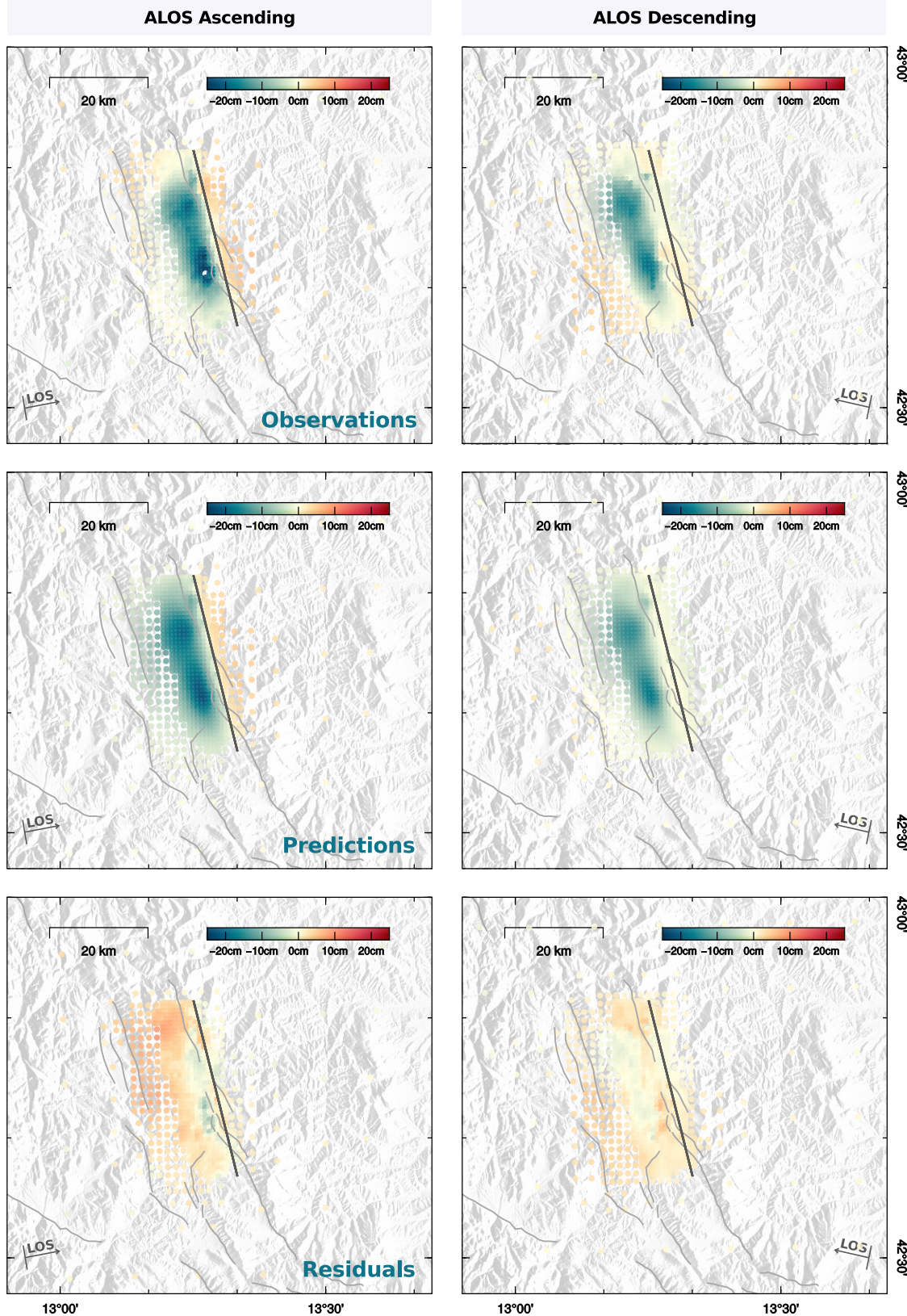


FIGURE S13 – Fit of the InSAR ALOS dataset for an inversion made assuming fault geometry A and accounting for C_p . Observations, predictions inferred from the average model and residuals are shown for ALOS 2 ascending and descending interferograms, respectively to the left and to the right. The assumed fault trace is shown with a dark gray line. Seismogenic faults are shown in light gray.

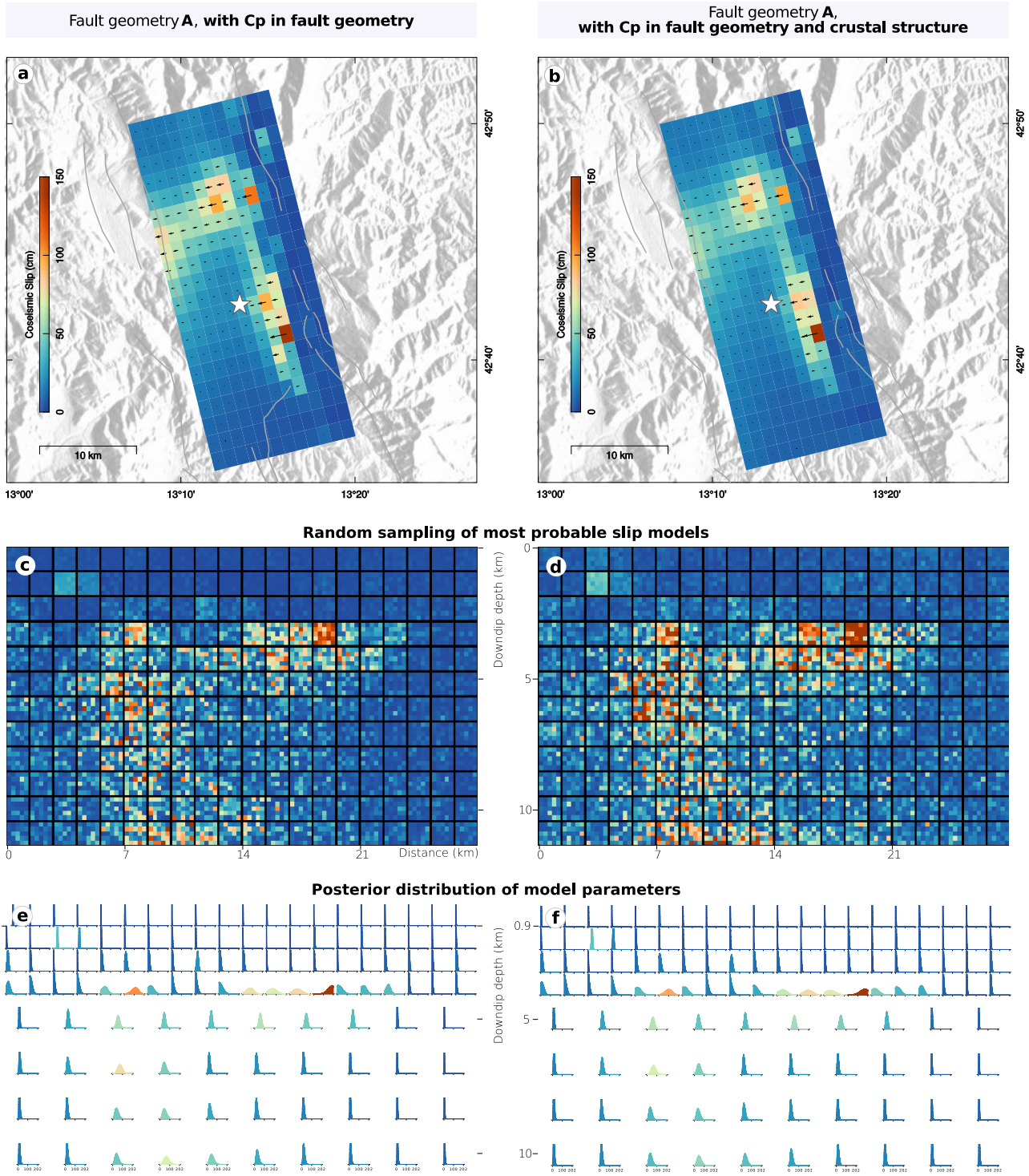


FIGURE S14 – Comparison of two finite-fault slip models inferred accounting for C_p in fault geometry (left) or for C_p in both fault geometry and crustal structure (right). (a) and (b) show the slip amplitude and rake of the average model, the epicenter being the white star. The color scale is valid for all the figures. (c) and (d) illustrate the slip amplitude of 25 random samples chosen among the most probable models. Each subfault (large square) thus contains 25 pixels colored according to the slip amplitude of the corresponding random sample. (e) and (f) represent the posterior marginal probability density functions.

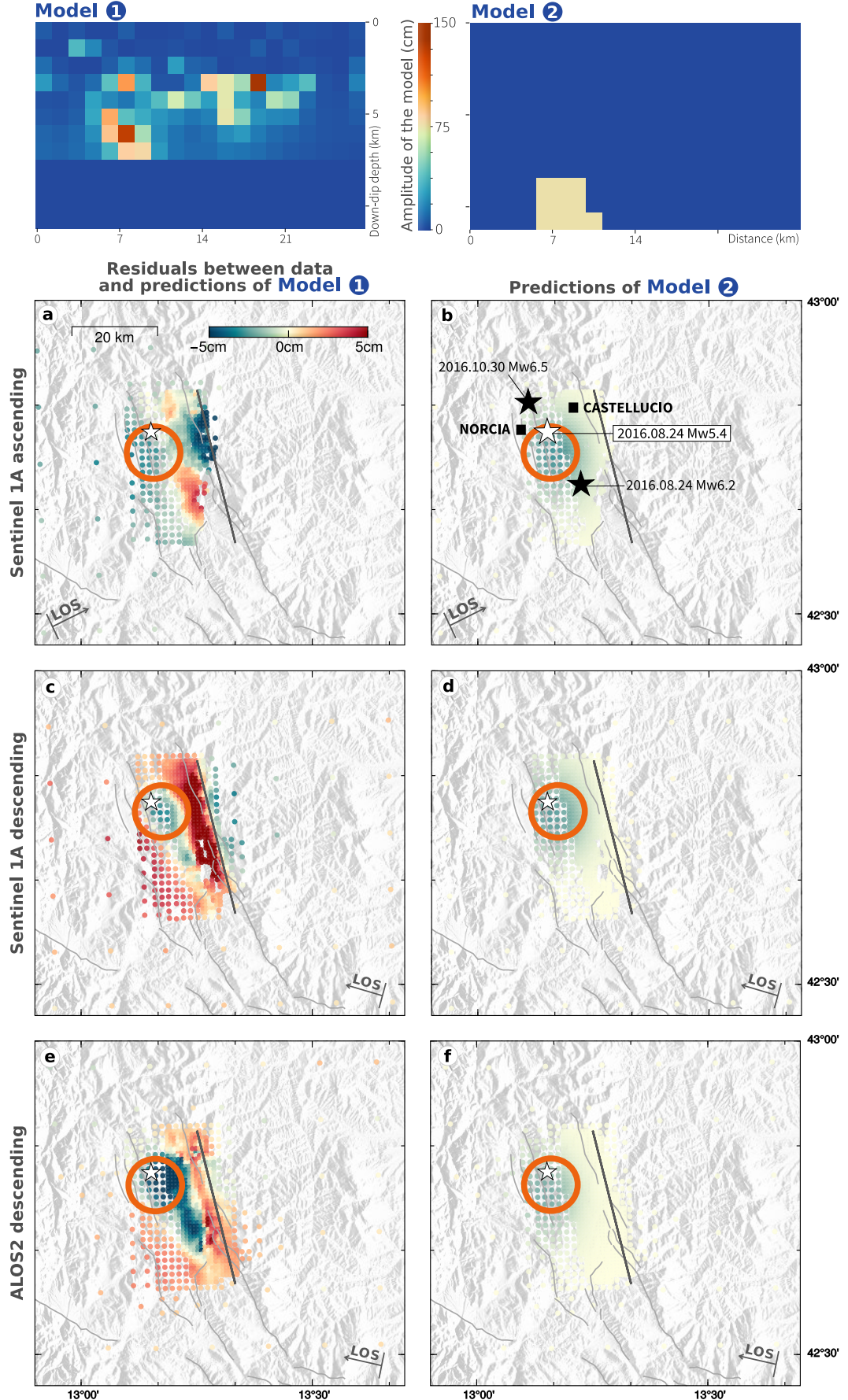


FIGURE S15 – The deep high slip area is required to explain some features of the InSAR data. Model (1) corresponds to the average model estimated assuming geometry A and without C_p , but with zero slip below 7 km depth. In contrast, Model (2) has subfaults slipping of 75 cm below 7 km depth, at the location of the deep high slip area, and no slip in other subfaults. (a), (c) and (e) show the residuals between the interferograms and the predictions of Model (1). (b), (d) and (f) show the predictions of Model (2) for the same interferograms and color-scale as in (a), (c) and (e). The red circle delineates the area with the largest predicted surface deformation using Model (2) –as in (b), (d) and (f)–, which corresponds to a deficit of surface deformation in the residuals plotted in (a), (c) and (e).

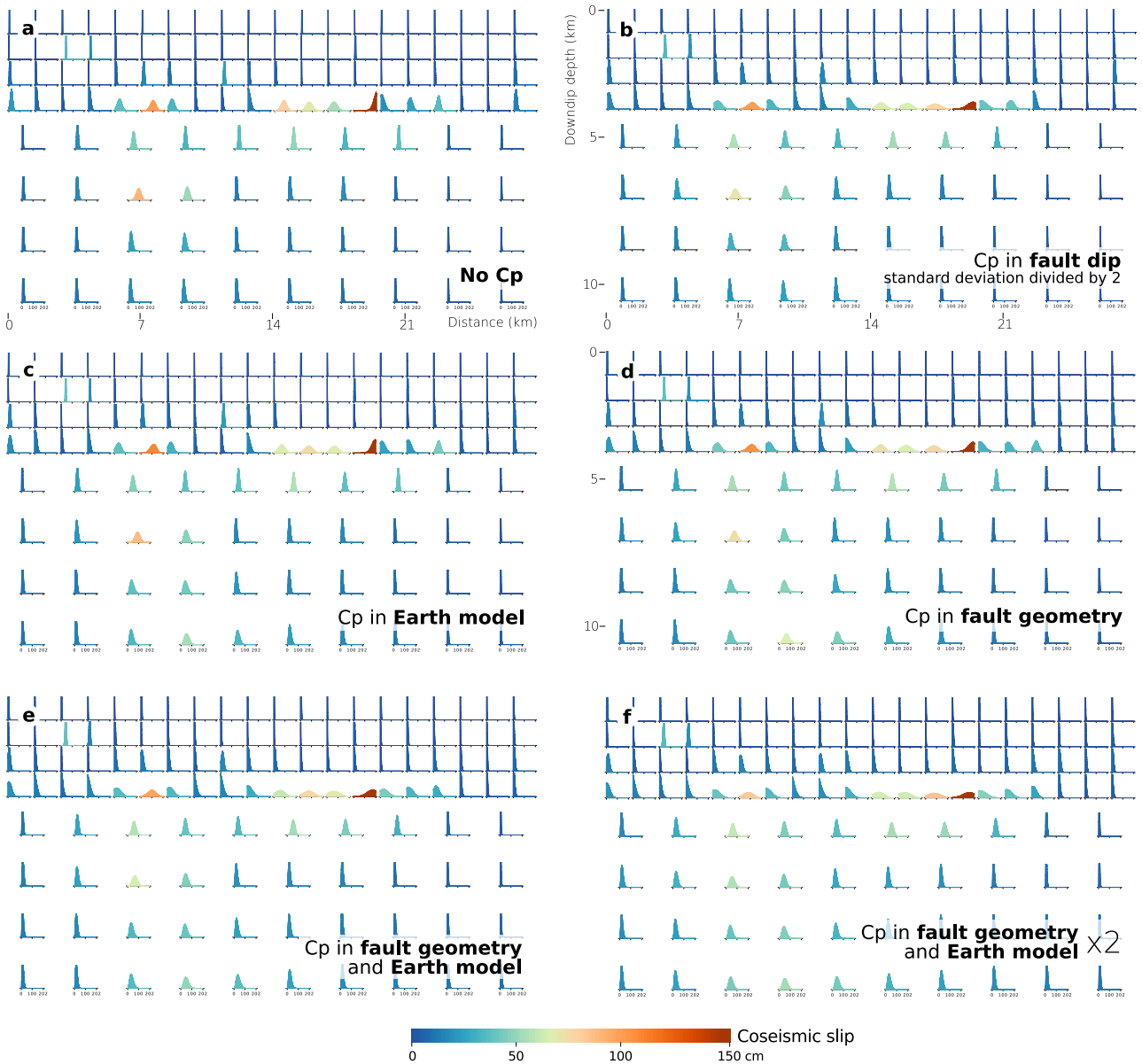


FIGURE S16 – Comparison of finite-fault slip models inferred accounting for different \mathbf{C}_p matrices (b-f) or not (a). Figures illustrate the posterior marginal PDFs for the 4 first rows and the mean of the posterior marginal PDFs over 2 subfaults along dip and two sub-faults along strike for the 4 last rows (i.e. the PDFs for doubled size subfaults). (a) No \mathbf{C}_p is accounted for (same model as in Fig. 2a). (b) Only $\mathbf{C}_p^{\text{dip}}$ is included, and the matrix has been computed with a prior standard deviation of 2.5° . (c) Only $\mathbf{C}_p^{\text{earth}}$ is introduced. (d) Only $\mathbf{C}_p^{\text{fault}}$ is accounted for (same model as in Fig. 6a). (e) Both $\mathbf{C}_p^{\text{fault}}$ and $\mathbf{C}_p^{\text{earth}}$ are accounted for (same model as in Fig. S14b). (f) Both $\mathbf{C}_p^{\text{fault}}$ and $\mathbf{C}_p^{\text{earth}}$ are accounted for such that $\mathbf{C}_p = 2 \times (\mathbf{C}_p^{\text{fault}} + \mathbf{C}_p^{\text{earth}})$.